Water-Dispersible Magnetite-Reduced Graphene Oxide Composites for Arsenic Removal

Vimlesh Chandra, Jaesung Park, Young Chun, Jung Woo Lee, In-Chul Hwang,* and Kwang S. Kim*

Center for Superfunctional Materials, Department of Chemistry, Pohang University of Science and Technology, Pohang 790-784, Korea

ABSTRACT Magnetite−graphene hybrids have been synthesized *via* a chemical reaction with a magnetite particle size of ~10 nm. The composites are superparamagnetic at room temperature and can be separated by an external magnetic field. As compared to bare magnetite particles, the hybrids show a high binding capacity for As(III) and As(V), whose presence in the drinking water in wide areas of South Asia has been a huge problem. Their high binding capacity is due to the increased adsorption sites in the M−RGO composite which occurs by reducing the aggregation of bare magnetite. Since the composites show near complete (over 99.9%) arsenic removal within 1 ppb, they are practically usable for arsenic separation from water.

KEYWORDS: arsenic removal · magnetite · superparamagnetic · graphene;

Arsenic is one of the most toxic and carcinogenic chemical elements when consumed in quantities (>10 ppb (parts per billion) which is the World Health Organization's standard) over a period.[1] Arsenic contamination of groundwater has led to a massive epidemic of arsenic poisoning in South and South East Asia.[2,3] It is estimated that 60 million people are drinking groundwater with arsenic concentrations above 10 ppb. Increased levels of skin cancer were associated with arsenic exposure in Wisconsin, even below 10 ppb.[4] Arsenic can be removed from drinking water through coprecipitation of iron minerals.[5] Using the highly specific surface area of Fe_3O_4 nanocrystals, the waste associated with arsenic removal from water has recently been substantially reduced.[6] Iron-oxide-based materials are very effective in the removal of heavy metal ions and arsenic (arsenate and arsenite).[7,8] However, these adsorbents are difficult to use in continuous flow systems due to small particle size and instability, since magnetite is highly susceptible to oxidation when exposed to the atmosphere.[9] To overcome this difficulty, several researchers have combined iron oxides with carbon[10,11] and carbon nanotubes.[12] Graphene-based materials such as graphene[13−15] and chemically modified graphene including graphene oxide (GO) have shown many applications in composite materials[16,17] and devices.[18−21] Chemical methods offer potentially low cost and large scale production of graphene-based hybrid materials.[22−24] Recently, magnetite−graphene oxide and magnetite−graphene hybrids have been synthesized and applied to targeted drug carriers and magnetic resonance imaging (MRI), respectively.[25,26] The large surface area and stability of the reduced graphene oxide (RGO) motivated us to synthesize magnetite−reduced graphene oxide (M−RGO) composites for arsenic removal. Here, we report a novel kind of magnetic composite based on RGO synthesized *in situ* at low temperatures (<100 °C). M−RGO composite shows nearly complete (over 99.9%) arsenic removal within 1 ppb, as a practical approach for arsenic separation from water.

RESULTS AND DISCUSSION

For the use of arsenic removal from water, we synthesized GO *via* Hummer's method,[22] and GO was exfoliated in water to produce a suspension of GO sheets. The mixed water solution of $FeCl_3$ and $FeCl_2$ was added slowly to the GO solution, and ammonia solution was added quickly to precipitate Fe^{2+}/Fe^{3+} ions for synthesis of magnetite (Fe_3O_4) nanoparticles. GO is reduced to RGO by hydrazine hydrate which was added slowly and stirred for 4 h at 90 °C. The dark-black colored solution was filtered and washed with water/ethanol and dried in vacuum at 70 °C. In this reaction process (Scheme 1), we synthesized Fe_3O_4−RGO (M−RGO) composites with different magnetite concentration. Here, we discuss

*Address correspondence to kim@postech.ac.kr (ksk), spfe@postech.ac.kr (ich).

Received for review April 26, 2010 and accepted June 11, 2010.

Published online June 16, 2010. 10.1021/nn1008897

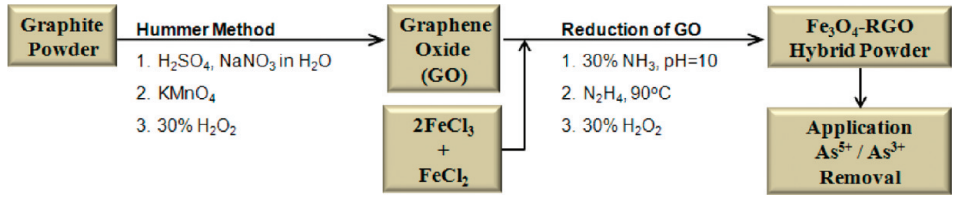

Scheme 1. Synthesis and application of Fe_3O_4−RGO composites

M1−RGO (0.7 g of GO, 0.4055 g of Fe^{3+} and 0.1584 g of Fe^{2+}) and M2−RGO (0.7 g of GO, 3.2442 g of Fe^{3+} and 1.2675 g of Fe^{2+}) having low and high concentrations of magnetite, respectively.

Powder X-ray diffraction (XRD) patterns were obtained and analyzed for graphite, graphene oxide, and as synthesized M−RGO composites (Supporting Information, Figure S1). The graphite shows a very sharp diffraction peak at 26.5° corresponding to a *d*-spacing of 0.336 nm (d_{002}). Oxidation treatment produces a decrease of the peak (002) intensity of graphite and the appearance of the diffraction peak of the graphene oxide at $2\theta = 14.8°$. M−RGO shows peaks corresponding to Fe_3O_4 (JCPDS No. 75-0033), and a broad peak appears at 23.9° which is attributed to reduced graphene oxide (RGO).[27] During growth of the M−RGO composite, the presence of magnetite reduces the aggregation of graphene sheets. The crystallite size of Fe_3O_4 nanoparticles in the graphene matrix is calculated from Scherrer's equation.[28] The wide scan XPS spectra of the M−RGO shows photoelectron lines at a binding energy of about 285, 530, and 711 eV attributed to C1s, O1s, and Fe2p, respectively (Figure 1a). In the spectrum of Fe2p (Figure 1b), the peaks $Fe2p_{3/2}$ and $Fe2p_{1/2}$ are located at 711.29 and 724.82 eV, not at 710.35 and 724.0 eV which are for γ-Fe_2O_3.[29] In addition, there is no satellite peak at ~719.0 eV, characteristic of γ-Fe_2O_3, which is indicative of formation of the Fe_3O_4 phase in the RGO matrix.[30] It is known that at least three types of oxygen species may contribute to the O1s peak[31] (Figure 1c), that is, the contribution of the anionic oxygen in Fe_3O_4 at about 530.2 eV, the oxygen containing functional groups at around 531.8 eV, and water at higher binding energies. The peak around 530.4 eV is due to the oxygen in the M−RGO, while the oxygen in graphene oxide is around 532.6 eV. Deconvolution of the C1s peak (Figure 1d) of graphene oxide shows the presence of different oxygen containing functional groups of (a) the non-oxygenated C at 284.8 eV, (b) the carbon in C−O at 286.2 eV, (c) the carbonyl carbon (C═O) at

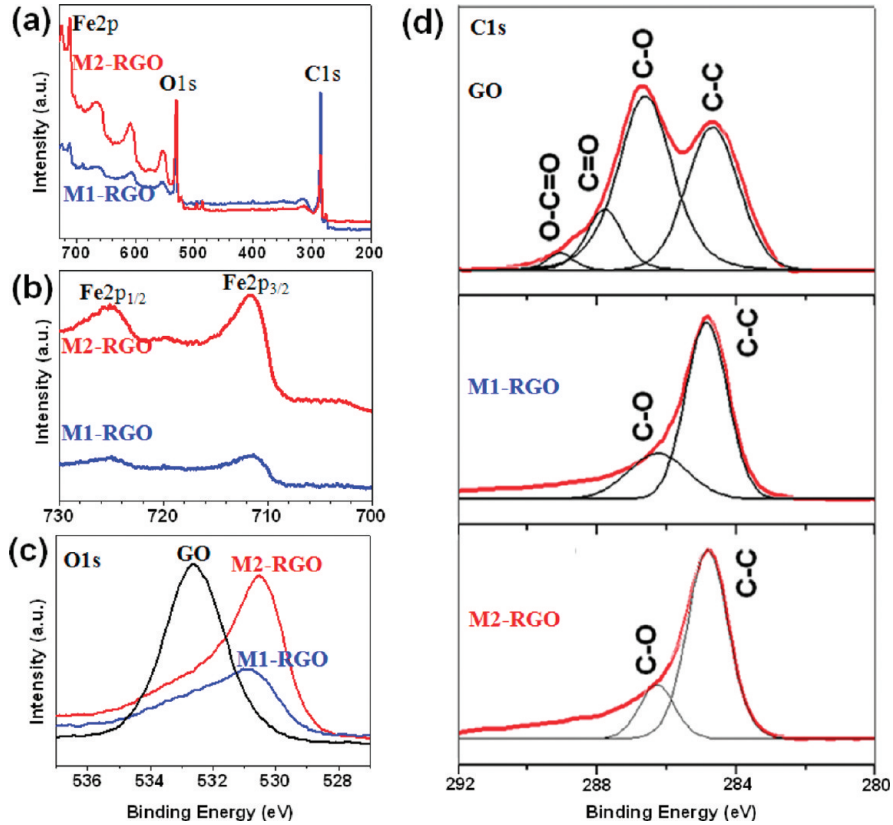

Figure 1. X-ray photoelectron spectroscopy (XPS) spectra: (a) wide scan, (b) Fe2p spectra, (c) O1s spectra, and (d) C1s spectra of graphene oxide (GO), of M1−RGO and M2−RGO.

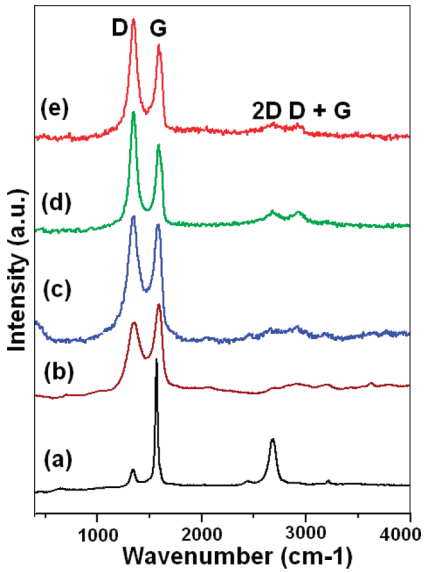

Figure 2. Raman spectra (λ = 532 nm) of (a) graphite, (b) graphene oxide, (c) graphene, (d) M1−RGO composite, and (e) M2−RGO composite. Note the change in intensity of D and G bands.

287.9 eV, and (d) the caboxylate carbon (O−C═O) at 289.0 eV. The C1s spectra of M−RGO show mainly the nonoxygenated carbon (284.8 eV) and the carbon in C−O (286.2 eV).

FTIR spectra (Supporting Information, Figure S2) of graphene oxide shows C═O (1719 cm^{-1}), aromatic C═C (1620 cm^{-1}), carboxyl C═O (1356 cm^{-1}), epoxy C−O (1217 cm^{-1}), and alkoxy C−O (1049 cm^{-1}) stretching vibrations. IR spectra of M−RGO show two broad peaks at 1556 and 1181 cm^{-1} which correspond to the aromatic C═C stretch and C−O stretch, respectively.[32] The transmittance band around 584 cm^{-1} is attributed to Fe−O,[33] and the enhanced intensity for Fe−O is indicative of high iron loading in M2−RGO.

In Figure 2, Raman spectra (532 nm excitation) of M−RGO displays two prominent peaks at ~1330 and ~1590 cm^{-1}, which correspond to the well-documented D band and G band, respectively. It is well-known that the G band corresponds to the first-order scattering of the E_{2g} mode observed for sp^2 carbon domains, and the pronounced D band is associated with structural defects, amorphous carbon, or edges that can break the symmetry and selection rule.[34] A universal observation is that higher disorder in graphite leads to a broader G band as well as to a broad D band of higher relative intensity compared to that of the G band. Therefore, the intensity ratio of D band to G band ($r = I_D/I_G$) is usually used as a measure of the disorder.[34] The intensity ratio (r) for M1−RGO (0.92), M2−RGO (1.28), and RGO (1.02) shows an enhanced value compared to that for GO (0.88), indicating the presence of localized sp^3 defects within the sp^2 carbon network upon reduction of the exfoliated GO.[35] The second order Raman feature, namely the 2D band at ~2600 cm^{-1}, is very sensitive to the stacking order of the graphene sheets along the c-axis as well as to the number of layers and

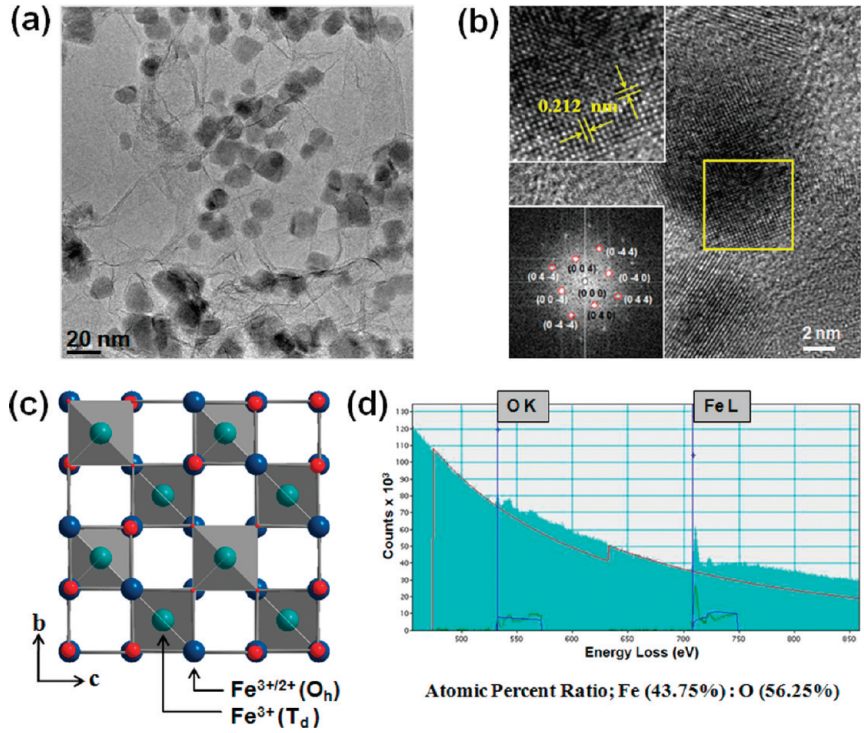

Figure 3. TEM analysis of Fe_3O_4 nanoparticles: (a) TEM image of M−RGO; (b) HRTEM image and selected area diffraction pattern of M−RGO where the top inset shows a close view of lattice fringes showing an interlayer distance of 0.212 nm corresponding to the (400) plane; (c) unit cell structure of Fe_3O_4-inverse spinel type where O_h and T_d correspond to octahedral ($Fe^{3+/2+}$) and tetrahedral (Fe^{3+}) polyhedron, respectively; (d) EELS spectrum of Fe_3O_4 nanoparticles in M−RGO with atomic ratios of Fe (43.75%) and O (56.25%), indicating the O K shell ionization edge and the FeL_2 and FeL_3 shell ionization edges.

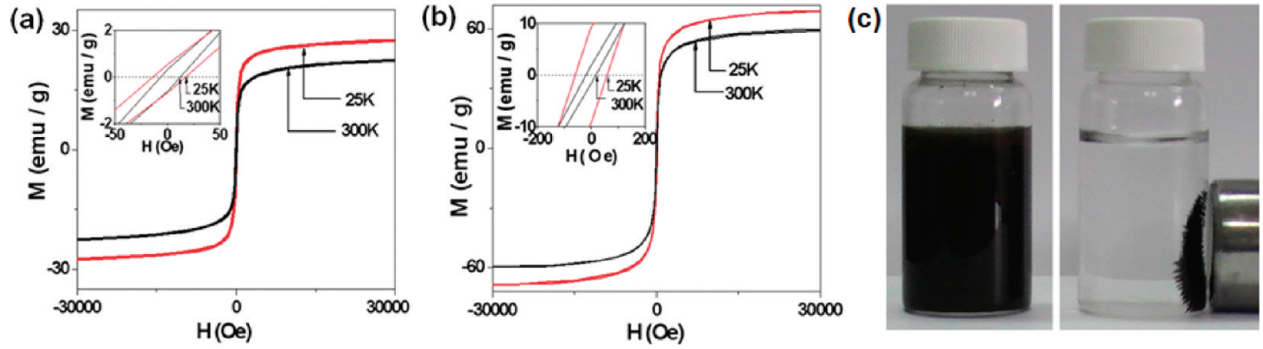

Figure 4. Hysteresis curves of M1−RGO (a) and M2−RGO (b) at 25 and 300 K (top inset shows close view of the hysteresis loops); (c) M−RGO composite dispersed water solution and magnetic separation.

shows more broadened shape (often a doublet) with an increasing number of graphene layers.[36,37] However, these specific features are not seen in our sample, where only a weakly smeared 2D band can be seen along with the D+G combination band induced by disorder at ~2930 cm^{-1}. Thus, it is conceivable that the sample contains highly disordered and randomly arranged graphene flakes.

The scanning electron microscope (SEM) images of the M−RGO composites (Supporting Information, Figure S3) show the presence of magnetite in RGO and crumpled sheets of RGO can be seen throughout the morphology. Energy dispersive X-ray spectroscopy (EDS) analysis shows the presence of C, O, and Fe. In Figure 3a, the TEM image of M1−RGO shows Fe_3O_4 nanoparticles well dispersed in the RGO matrix with the average particle size of 11 nm, and the graphene sheets showing the folding nature are clearly visible. The Fe_3O_4 nanoparticles are not simply mixed up or blended with RGO; rather, they are entrapped inside the RGO sheets. In Figure 3b, the HRTEM image shows lattice fringes from Fe_3O_4 nanoparticles in the surrounding of the RGO matrix. The lattice spacing is 0.212 nm which corresponds to the indexes (400, 040, and 004) reflections. The selected area diffraction (SAED) pattern shows that the nanocrystalline structure of magnetite grows along [001]. These values give an estimated lattice parameter in good agreement with the reference (a = 8.384 Å, JCPDS No. 75-0033). The unit cell of inverse spinel type magnetite (Fe_3O_4) has a close-packed tetragonal structure with two kinds of interstitial sites, tetrahedral (Td) and octahedral (Oh) sites, which are surrounded by 4 and 6 oxygen ions, respectively (Figure 3c). To clarify the chemical composition of Fe_3O_4 nanoparticles in RGO sheets, the energy-loss spectroscopy (EELS) analysis is shown in Figure 3d. It reveals the characteristic oxygen K shell ionization edge (~532 eV, ~542 eV) and the ionization edge (~712 eV, ~726 eV) corresponding to the FeL_2 and FeL_3 shells, respectively. From the quantitative STEM-EELS analysis, it demonstrates that the atomic ratio of Fe to O is 3:4, which further confirms the formation of Fe_3O_4 nanoparticles in RGO.

The STEM-HAADF (high angle annular dark field) image and EDS mapping images of M1−RGO shows homogeneous distribution of iron, carbon, and oxygen in the entire range, while tapping mode AFM image shows that the thickness of GO sheets is ~1.2 nm and that of graphene sheet in M−RGO is ~4 nm (Supporting Information, Figures S4 and S6).

Magnetic properties of the M−RGO composites were studied with superconducting quantum interference device (SQUID). The zero field cooling (ZFC) and field cooling (FC) measurement of the temperature dependence of magnetization (Supporting Information, Figure S7) shows superparamagnetism character of the magnetite nanoparticles and blocking temperature (T_B) for M1−RGO (96 K) and for M2−RGO (112 K). These values are expected to correspond to magnetite nanoparticles sizes of ~11 nm.[38]

The magnetic hysteresis curves were recorded at 300 K (room temperature) and 25 K (Figure 4a,b). The saturation magnetization ($\mathbf{M}_S$), remanence ($\mathbf{M}_R$), and coercivity for M−RGO are summarized in Table 1. The magnetic intensities are lower than bulk Fe_3O_4 due to the presence of RGO and the small size of Fe_3O_4 nanoparticles. The M−RGO composites exhibit a superparamagnetic state with small remnant magnetization and coercivity at room temperature which is desirable for many practical applications, so that strong magnetic signals at small applied magnetic fields are obtained.

TABLE 1. Average Particle Diameters (d in nm) Calculated from TEM and X-ray Data, Saturation Magnetization (M_S), Coercive Field (H_C), Remanence M_R for M−RGO Composites at 25 and 300 K

			H_C (Oe)		M_R (emu/g)		M_S (emu/g)		
sample	TEM d (nm)	XRD d (nm)	25 K	300 K	25 K	300 K	25 K	300 K	T_B(K)
M1−RGO	11	8.6	18	12.0	0.5	0.3	27.4	22.3	96
M2−RGO	12	9.4	60	19.6	9.1	1.7	69.0	59.0	112

TABLE 2. Langmuir and Freundlich Adsorption Isotherm Parameters for As(III) and As(V) on M−RGO

		M2−RGO		M1−RGO	
isotherm type	isotherm constants	As(V)	As(III)	As(V)	As(III)
Langmuir	*a* (mg/g)	5.83	13.10	5.27	10.20
	b (L/mg)	0.42	0.28	0.40	0.27
Freundlich	*k*	2.28	3.79	1.99	2.90
	n	2.95	2.32	2.88	2.29

The M1−RGO composites dispersed in water solution (1 mg/mL) can be separated from water by using a magnet (Figure 4c). The separation is almost completed in ~10 s in the applied magnetic field of ~20 mT (Supporting Information, Figure S8 and Movie). Surface area measurement of the M−RGO *via* nitrogen gas absorption yielded a Brunauer, Emmett and Teller (BET) surface area of 148 m^2/g for M1−RGO and 117 m^2/g for M2−RGO (Supporting Information: Figure S9). The surface area of magnetite in M−RGO decreases with increasing magnetite loading in RGO.

Aqueous solutions with different initial arsenic concentrations varying from 3 to 7 ppm were used for the experiment at neutral pH = 7, adsorption time 2 h, and T = 20 °C as shown in Figure 5a. The data of arsenic adsorption were fitted with *Freundlich*[39] and *Langmuir isotherm* models.[40] The Langmuir isotherm is expressed as follows:

$$q_e = abC_e/(1 + bC_e) \quad (1)$$

The Freundlich isotherm is represented by the following equation:

$$q_e = k(C_e)^{1/n} \quad (2)$$

where q_e is the amount of arsenic adsorbed per unit weight of adsorbent (mg/g), C_e is the equilibrium concentration of arsenic (mg/L), b is the constant related to the free energy of adsorption (L/mg), and a is the maximum adsorption capacity (mg/g). The Freundlich constant (k) is indicative of the relative adsorption capacity of the adsorbent (mg/g), and ($1/n$) is the adsorption intensity.

A nonlinear fitting was applied to obtain all Langmuir and Freundlich isotherm parameters. Adsorption data fit Langmuir and Freundlich isotherms well ($R^2 >$ 0.97). The adsorption constants evaluated from the isotherms for M−RGO are listed in Table 2. The Freundlich constant n is found to be greater than 1 which is a favorable condition for adsorption. The maximum adsorption capacity for arsenic ions is shown in a diagram in Figure 5b. The removal capacity of As(III) is higher than that of As(V) with M−RGO. The arsenic removal capacity of arsenic with M2−RGO is higher than that with the M1−RGO. Such type of effects were reported in ferric-oxide-loaded polymeric sorbents.[41]

The kinetics of arsenic ions removal was determined in order to understand the adsorption behavior of the

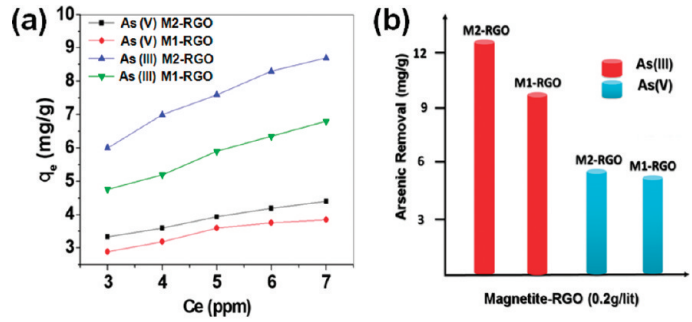

Figure 5. (a) Adsorption isotherms of As(III) and As(V) on the Fe_3O_4−RGO composite (temperature 20 °C, pH 7). (b) Maximum adsorption capacity of M−RGO composites for arsenic removal from water.

M−RGO composites. Figure 6 shows the adsorption data of arsenic ions by M−RGO at different time intervals. The kinetic data for the sorbent were fitted to a pseudo-second-order kinetic model.

The kinetic rate equation is expressed as

$$dq_t/dt = k_2(q_e - q_t)^2 \quad (3)$$

where q_e is the sorption capacity at equilibrium and q_t is the solid-phase loading of arsenic at time t. The k_2 ($mL \cdot mg^{-1} \cdot min^{-1}$) represents the pseudo-second-order rate constant for the kinetic model.[42,43] By integrating eq 3 with the boundary conditions of $q_t = 0$ at $t = 0$ and $q_t = q_t$ at $t = t$, the following linear equation can be obtained:

$$t/q_t = k_2/q_e^2 + 1/q_e t \quad (4)$$

$$V_0 = k_2 q_e^2$$

where V_0 ($mg \cdot mL^{-1} \cdot min^{-1}$) is the initial sorption rate. Therefore, the V_0 and q_e values of kinetic tests can be determined experimentally by plotting the t/q_t *versus* t. The results in Table 3 indicate that As(III) uptake onto M−RGO is favorable by the pseudo-second-order kinetic model.

The temperature effect on arsenic ions removal is depicted in Figure 7. The experiment condition of pH 7, adsorption time of 120 min, adsorbent dose of 0.2 g/L and arsenic ions concentration of 5 ppm were kept as constant parameters, while the temperature was varied from 10 to 50 °C. Arsenic ions removal increases when temperature increases from 10 to 30 °C, while on further increase in temperature the arsenic removal

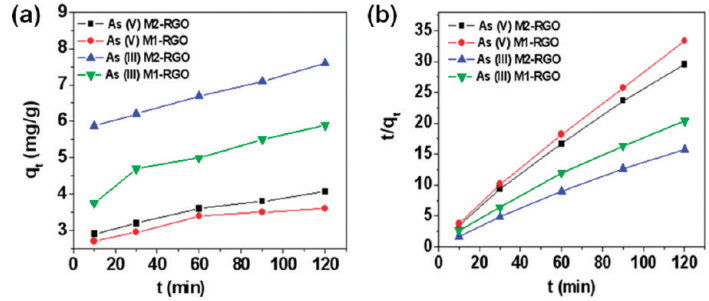

Figure 6. Kinetic absorption data plots of arsenic ions by M−RGO: (a) arsenic removal rate q_t *vs* time t and (b) the transformed rate plot t/q_t *vs* t.

TABLE 3. Parameters of a Pseudo-second-order Kinetic Model Fitting Arsenic Adsorption Kinetics

sorbent	isotherm constant	As(V)	As(III)
M2−RGO	q_e	4.23	7.81
	k_2	0.029	0.02
	V_0	0.53	1.23
M1−RGO	q_e	3.35	6.21
	k_2	0.041	0.017
	V_0	0.59	0.64

decreases. Pokhrel *et al.*[44] observed an increase in arsenic removal from 5 to 30 °C and Mondal *et al.*[45] reported a decrease in arsenic removal from 30 to 60 °C. The temperature of the maximum arsenic ions adsorption is at 30 °C.

The pH effect on the arsenic ion adsorption by M−RGO is shown in Figure 8. Arsenic ion removal on the M−RGO surface is due to the electrostatic attraction between the positively charged surface of M−RGO and the negatively charged arsenic/arsenous acid. Under most pH conditions, As(V) is present in negative ionic form ($H_2AsO_3^-$), whereas As(III) is in a nonionic form (H_3AsO_4).[46] The pH-value dependence of arsenic ions adsorption onto M−RGO can be explained by point of zero charge (pH_{PZC}) of the adsorbent. At pH < pH_{PZC}, the M−RGO surface is positively charged, whereas at a pH > pH_{PZC}, the M−RGO surface is negatively charged. Due to the net positive surface charge of M−RGO at a pH < pH_{PZC}, it attracts As(V) anions, resulting in large adsorption at a low pH-value. As pH-value increases, the positively charged surface sites on the M−RGO decrease, causing a reduction in As(V) adsorption. Similar results were also obtained by Guo *et al.*,[47] who investigated the adsorption of arsenate on cellulose loaded with iron oxyhydroxide. For As(III), as pH-value increases, the amount of negatively charged arsenic species rises, while positively charged surface sites decrease up to the pH_{ZFC}-value. The increase in the adsorption of As(III) in alkaline solutions suggests that the electrostatic factors do not control the adsorption process onto M−RGO. The strong adsorption of arsenic at pH > pH_{PZC} indicates that the adsorption process is followed by surface complexation, rather than electrostatic interactions. Guo *et al.* also observed such type of adsorption for As(III) on cellulose loaded with iron oxyhydroxide.[47]

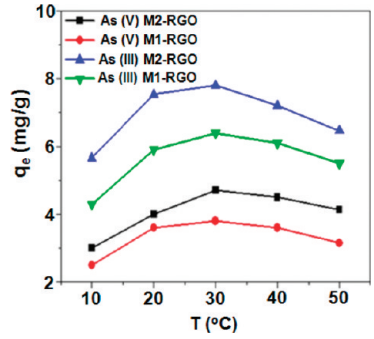

Figure 7. Effect of temperature on arsenic adsorption: pH, 7; adsorption time, 2 hours; adsorbent dose, 0.2 g/L; and arsenic concentration, 5 ppm.

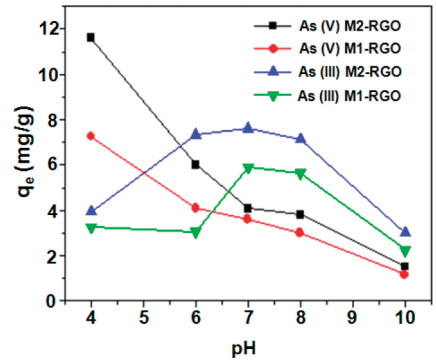

Figure 8. Effect of pH on arsenic adsorption: temperature, 20 °C; adsorption time, 2 h; adsorbent dose, 0.2 g/L; and arsenic concentration, 5 ppm.

CONCLUSION

To get rid of arsenic from water, we have employed magnetite−reduced graphene oxide (M−RGO) composites *via* a chemical reaction with magnetite particle size average of ~10 nm. M−RGO composites are superparamagnetic at room temperature and can be separated by an external magnetic field. These composites show high binding capacity for As(III) and As(V), due to increased adsorption sites in the presence of reduced graphene oxide. The composites show near complete (over 99.9%) arsenic removal within 1 ppb. Thus, they are practically usable for arsenic separation from water.

METHODS

The details of experiments are given in Supporting Information. In brief, GO was synthesized by using the Hummers method[22] through oxidation of graphite powder. The Fe_3O_4−RGO composites were synthesized using ammonia solution (30%) and hydrazine hydrate at a temperature of 90 °C and pH = 10. The arsenic concentrations prior to and after adsorption were determined by an inductively coupled plasma-emission spectrometer (ICP-ES).

Acknowledgment. This work was supported by NRF (National Scientist program, EPB Center: 2009-0063312, GRL, WCU: *R*32-2008-000-10180-0) and POSCO (StSc-4003589).

Supporting Information Available: Experiment details: synthesis, XRD, FTIR, SEM, TEM, AFM, ZFC-FC, magnetite separation movie, and BET surface area data. This material is available free of charge *via* the Internet at http://pubs.acs.org.

REFERENCES AND NOTES

1. Mohan, D.; Pittman, C. U., Jr. Arsenic Removal from Water/Wastewater Using Adsorbents—A Critical Review. *J. Hazard. Mater.* **2007**, *142*, 1–53.
2. Meharg, A. EarthV. Venomous Earth: How Arsenic Caused The World's Worst Mass Poisoning; Macmillan: Houndsmill, England, 2005.
3. Polizzotto, M. L.; Kocar, B. D.; Benner, S. G.; Sampson, M.;

Fendorf, S. Near-Surface Wetland Sediments as a Source of Arsenic Release to Ground Water in Asia. *Nature* **2008**, *454*, 505–509.
4. Knobeloch, L. M.; Zierold, K. M.; Anderson, H. A. Association of Arsenic-Contaminated Drinking-Water With Prevalence of Skin Cancer in Wisconsin's Fox River Valley. *J. Health Popul. Nutr.* **2006**, *24*, 206–213.
5. Meng, X.; Korfiatis, G. P.; Christodoulatos, C.; Bang, S. Treatment of Arsenic in Bangladesh Well Water Using a Household Co-precipitation and Filtration System. *Water Res.* **2001**, *35*, 2805–2810.
6. Yavuz, C. T.; Mayo, J. T.; Yu, W. W.; Prakash, A.; Falkner, J. C.; Yean, S.; Cong, L.; Shipley, H. J.; Kan, A.; Tomson, M.; Natelson, D.; Colvin, V. L. Low-Field Magnetic Separation of Monodisperse Fe_3O_4 Nanocrystals. *Science* **2006**, *314*, 964–967.
7. Shin, S.; Jang, J. Thiol Containing Polymer Encapsulated Magnetic Nanoparticles as Reusable and Efficiently Separable Adsorbent for Heavy Metal Ions. *Chem. Commun.* **2007**, 4230–4232.
8. Sarkar, S.; Blaney, L. M.; Gupta, A.; Ghosh, D.; Gupta, A. K. S. Arsenic Removal from Groundwater and Its Safe Containment in a Rural Environment: Validation of a Sustainable Approach. *Environ. Sci. Technol.* **2008**, *42*, 4268–4273.
9. Jolivet, J.-P.; Chaneac, C.; Tronc, E. Iron Oxide Chemistry. From Molecular Clusters to Extended Solid Networks. *Chem. Commun.* **2004**, 481–487.
10. Zhang, S.; Li, X.; Chen, J. P. Preparation and Evaluation of a Magnetite-Doped Activated Carbon Fiber for Enhanced Arsenic Removal. *Carbon* **2010**, *48*, 60–67.
11. Mauter, M. S.; Elimelech, M. Environmental Applications of Carbon-Based Nanomaterials. *Environ. Sci. Technol.* **2008**, *42*, 5843–5859.
12. Miyamoto, J.; Kanoh, H.; Kaneko, K. The Addition of Mesoporosity to Activated Carbon Fibers by a Simple Reactivation Process. *Carbon* **2005**, *43*, 855–857.
13. Novoselov, K. S.; Geim, A. K.; Morozov, S. V.; Jiang, D.; Zhang, Y.; Dubonos, S. V.; Grigorieva, I. V.; Firsov, A. A. Electric Field Effect in Atomically Thin Carbon Films. *Science* **2004**, *306*, 666–669.
14. Kim, K. S.; Zhao, Y.; Jang, H.; Lee, S. Y.; Kim, J. M.; Kim, K. S.; Ahn, J.-H.; Kim, P.; Choi, J.-Y.; Hong, B. H. Large-Scale Pattern Growth of Graphene Films for Stretchable Transparent Electrodes. *Nature* **2009**, *457*, 706–710.
15. Li, X.; Cai, W.; An, J.; Kim, S.; Nah, J.; Yang, D.; Piner, R.; Velamakanni, A.; Jung, I.; Tutuc, E.; *et al*. Large-Area Synthesis of High-Quality and Uniform Graphene Films on Copper Foils. *Science* **2009**, *324*, 1312–1314.
16. Ramanathan, T.; Abdala, A. A.; Stankovich, S.; Dikin, D. A.; Alonso, M. H.; Piner, R. D.; Adamson, D. H.; Schniepp, H. C.; Chen, X.; Ruoff, R. S.; *et al*. Functionalized Graphene Sheets for Polymer Nanocomposites. *Nat. Nanotechnol.* **2008**, *3*, 327–331.
17. Scheuermann, G. M.; Rumi, L.; Steurer, P.; Bannwarth, W.; Malhaupt, R. Palladium Nanoparticles on Graphite Oxide and Its Functionalized Graphene Derivatives as Highly Active Catalysts for the Suzuki–Miyaura Coupling Reaction. *J. Am. Chem. Soc.* **2009**, *131*, 8262–8270.
18. Schedin, F.; Geim, A. K.; Morozov, S. V.; Hill, E. W.; Blake, P.; Katsnelson, M. I.; Novoselov, K. S. Detection of Individual Gas Molecules Adsorbed on Graphene. *Nat. Mater.* **2007**, *6*, 652–655.
19. Kim, W. Y.; Kim, K. S. Prediction of Very Large Values of Magnetoresistance in a Graphene Nanoribbon Device. *Nat. Nanotechnol.* **2008**, *3*, 408–412.
20. Wang, X.; Zhi, L.; Mullen, K. Transparent, Conductive Graphene Electrodes for Dye-Sensitized Solar Cells. *Nano Lett.* **2008**, *8*, 323–327.
21. Yu, Y. J.; Zhao, Y.; Ryu, S.; Brus, L.; Kim, K. S.; Kim, P. Charge Transfer Chemical Doping of Few Layer Graphenes: Charge Dirstribution and Band Gap Formation. *Nano Lett.* **2009**, *9*, 3430–3434.
22. Hummers, W. S.; Offeman, R. E. Preparation of Graphitic Oxide. *J. Am. Chem. Soc.* **1958**, *80*, 1339.
23. Stankovich, S.; Dikin, D. A.; Dommett, G. H. B.; Kohlhaas, K. A.; Zimney, E. J.; Stach, E. A.; Piner, R. D.; Nguyen, S. T.; Ruoff, R. S. Graphene-Based Composite Materials. *Nature* **2006**, *420*, 282–286.
24. Myung, S.; Park, J.; Lee, H.; Kim, K. S.; Hong, S. Ambipolar Memory Devices Based on Reduced Graphene Oxide and Nanoparticles. *Adv. Mater.* **2010**, *22*, 2045–2049.
25. Yang, X.; Zhang, X.; Ma, Y.; Huang, Y.; Wang, Y.; Chen, Y. Superparamagnetic Graphene Oxide–Fe_3O_4 Nanoparticles Hybrid for Controlled Targeted Drug Carriers. *J. Mater. Chem.* **2009**, *19*, 2710–2714.
26. Cong, H. P.; He, J. J.; Lu, Y.; Yu, S. H. Water-Soluble Magnetic-Functionalized Reduced Graphene Oxide Sheets: *In Situ* Synthesis and Magnetic Resonance Imaging Applications. *Small* **2009**, *6*, 169–171.
27. Zhu, Y.; Stoller, M.I. D.; Cai, W.; Velamakanni, A.; Piner, R. D.; Chen, D.; Ruoff, R. S. Exfoliation of Graphite Oxide in Propylene Carbonate and Thermal Reduction of the Resulting Graphene Oxide Platelets. *ACS Nano* **2010**, *4*, 1227–1233.
28. Cullity, B. D. Stock, S. R. *Elements of X-Ray Diffraction*, 3rd ed.; Prentice-Hall, NJ, 2001.
29. Lu, J.; Jiao, X.; Chen, D.; Li, W. Solvothermal Synthesis and Characterization of Fe_3O_4 and γ-Fe_2O_3 Nanoplates. *J. Phys. Chem. C* **2009**, *113*, 4012–4017.
30. Zhang, D.; Liu, Z.; Han, S.; Li, C.; Lei, B.; Stewart, M. P.; Tour, J. M.; Zhou, C. Magnetite (Fe_3O_4) Core–Shell Nanowires: Synthesis and Magnetoresistance. *Nano Lett.* **2004**, *4*, 2151–2155.
31. Xia, W.; Chen, X.; Kundu, S.; Wang, X.; Grundmeier, G.; Wang, Y.; Bron, M.; Schuhmann, W.; Muhler, M. Chemical Vapor Synthesis of Secondary Carbon Nanotubes Catalyzed by Iron Nanoparticles Electrodeposited on Primary Carbon Nanotubes. *Surf. Coat. Technol.* **2007**, *201*, 9232–9237.
32. Park, S.; An, J.; Jung, I.; Piner, R. D.; An, S. J.; Li, X.; Velamakanni, A.; Ruoff, R. S. Colloidal Suspensions of Highly Reduced Graphene Oxide in a Wide Variety of Organic Solvents. *Nano Lett.* **2009**, *9*, 1593–1597.
33. Waldron, R. D. Infrared Spectra of Ferrites. *Phys. Rev.* **1955**, *99*, 1727–1735.
34. Ferrari, A. C.; Robertson, J. Interpretation of Raman Spectra of Disordered and Amorphous Carbon. *Phys. Rev. B* **2000**, *61*, 14095–14107.
35. Tuinstra, F.; Koenig, J. L. Raman Spectrum of Graphite. *J. Chem. Phys.* **1970**, *53*, 1126–1130.
36. Ferrari, A. C.; Meyer, J. C.; Scardaci, V.; Casiraghi, C.; Lazzeri, M.; Mauri, F.; Piscanec, S.; Jiang, D.; Novoselov, K. S.; Roth, S.; Geim, A. K. Raman Spectrum of Graphene and Graphene Layers. *Phys. Rev. Lett.* **2006**, *97*, 187401–187404.
37. Pimenta, M. A.; Dresselhaus, G.; Dresselhaus, M. S.; Cancado, L. A.; Jorio, A.; Sato, R. Studying Disorder in Graphite-Based Systems by Raman Spectroscopy. *Phys. Chem. Chem. Phys.* **2007**, *9*, 1276–1291.
38. Goya, G. F.; Berquo, T. S.; Fonseca, F. C.; Morales, M. P. Static and Dynamic Magnetic Properties of Spherical Magnetite Nanoparticles. *J. Appl. Phys.* **2003**, *94*, 3520–3528.
39. Langmuir, I. The Adsorption of Gases on Plane Surfaces of Glass, Mica, and Platinum. *J. Am. Chem. Soc.* **1918**, *40*, 1361–1403.
40. Freundlich, H. M. F. Zeitschrift fuer Physikalische Chemie, Stoechiometrie und Verwandtschaftslehre. *J. Phys. Electrochem.* **1906**, *57*, 385–470.
41. Zhang, Q.; Pan, B.; Zhang, W.; Pan, B.; Zhang, Q.; Ren, H. Arsenate Removal from Aqueous Media by Nanosized Hydrated Ferric Oxide (HFO)-Loaded Polymeric Sorbents: Effect of HFO Loadings. *Ind. Eng. Chem. Res.* **2008**, *47*, 3957–3962.
42. Kim, Y.; Kim, C.; Choi, I.; Rengaraj, S.; Yi, J. Arsenic Removal Using Mesoporous Alumina Prepared *via* a Templating Method. *Environ. Sci. Technol.* **2004**, *38*, 924–931.
43. Jang, M.; Shin, E. W.; Park, J. K.; Choi, S. I. Mechanisms of Arsenate Adsorption by Highly-Ordered Nanostructured

Silicate Media Impregnated with Metal Oxides. *Environ. Sci. Technol.* **2003**, *37*, 5062–5070.
44. Pokhrel, D.; Viraraghavan, T. Arsenic Removal from an Aqueous Solution by Modified *A. Niger* Biomass: Batch Kinetic and Isotherm Studies. *J. Hazard. Mater.* **2008**, *150*, 818–825.
45. Mondal, P.; Balomajumder, C.; Mohanty, B. A Laboratory Study for the Treatment of Arsenic, Iron and Manganese Bearing Groundwater Using Fe^{3+} Impregnated Activated Carbon: Effects of Shaking Time, pH, and Temperature. *J. Hazard. Mater.* **2007**, *144*, 420–426.
46. Lin, T. F.; Wu, J. K. Adsorption of Arsenite and Arsenate within Activated Alumina Grains: Equilibrium and Kinetics. *Water Res.* **2001**, *35*, 2049–2057.
47. Guo, X.; Chen, F. Removal of Arsenic by Bead Cellulose Loaded with Iron Oxyhydroxide from Groundwater. *Environ. Sci. Technol.* **2005**, *39*, 6808–6818.